

**Award Number:** W81XWH-10-1-0836

**TITLE:** Challenges of Zinc-Specific Transrectal  
Fluorescence Tomography to Detect Prostate Cancer

**PRINCIPAL INVESTIGATOR:** Anqi Zhang

**CONTRACTING ORGANIZATION:** Oklahoma State University  
Stillwater, Oklahoma 74078

**REPORT DATE:** October 2012

**TYPE OF REPORT:** Annual Summary

**PREPARED FOR:** U.S. Army Medical Research and Materiel Command  
Fort Detrick, Maryland 21702-5012

**DISTRIBUTION STATEMENT:**

Approved for public release; distribution unlimited

The views, opinions and/or findings contained in this report are those of the author(s) and should not be construed as an official Department of the Army position, policy or decision unless so designated by other documentation.

<b>REPORT DOCUMENTATION PAGE</b>				<b>Form Approved OMB No. 0704-0188</b>	
<small>Public reporting burden for this collection of information is estimated to average 1 hour per response, including the time for reviewing instructions, searching data sources, gathering and maintaining the data needed, and completing and reviewing the collection of information. Send comments regarding this burden estimate or any other aspect of this collection of information, including suggestions for reducing this burden to Washington Headquarters Service, Directorate for Information Operations and Reports, 1215 Jefferson Davis Highway, Suite 1204, Arlington, VA 22202-4302, and to the Office of Management and Budget, Paperwork Reduction Project (0704-0188) Washington, DC 20503.</small>					
<b>PLEASE DO NOT RETURN YOUR FORM TO THE ABOVE ADDRESS.</b>					
<b>1. REPORT DATE (DD-MM-YYYY)</b> 1 October 2012		<b>2. REPORT TYPE</b> Annual Summary		<b>3. DATES COVERED (From - To)</b> 15 Sep 2011 - 14 Sep 2012	
<b>4. TITLE AND SUBTITLE</b> Challenges of Zinc-Specific Transrectal Fluorescence Tomography to Detect Prostate Cancer				<b>5a. CONTRACT NUMBER</b>	
				<b>5b. GRANT NUMBER</b> W81XWH-10-1-0836	
				<b>5c. PROGRAM ELEMENT NUMBER</b>	
<b>6. AUTHOR(S)</b> Anqi Zhang (Pre-doctoral trainee PI) Daqing Piao (Mentor)  daqing.piao@okstate.edu				<b>5d. PROJECT NUMBER</b>	
				<b>5e. TASK NUMBER</b>	
				<b>5f. WORK UNIT NUMBER</b>	
<b>7. PERFORMING ORGANIZATION NAME(S) AND ADDRESS(ES)</b> Oklahoma State University Stillwater, Oklahoma 74078				<b>8. PERFORMING ORGANIZATION REPORT NUMBER</b>	
<b>9. SPONSORING/MONITORING AGENCY NAME(S) AND ADDRESS(ES)</b> U.S. Army Medical Research and Materiel Command Fort Detrick, Maryland 21702-5012				<b>10. SPONSOR/MONITOR'S ACRONYM(S)</b>	
				<b>11. SPONSORING/MONITORING AGENCY REPORT NUMBER</b>	
<b>12. DISTRIBUTION AVAILABILITY STATEMENT</b> Approved for public release; distribution unlimited					
<b>13. SUPPLEMENTARY NOTES</b>					
<b>14. ABSTRACT</b> In the year-2, we advanced our understandings regarding the challenges of trans-rectal fluorescence diffuse optical tomography (FDOT) of negative-contrast targets, for prostate cancer detection by using zinc-specific fluorescent probe. The challenges are evaluated through analytical, numerical, and experimental methods. Specifically, <ul style="list-style-type: none"> <li>• we developed a novel analytical approach to quantify diffuse photon propagation in an outward-imaging geometry that idealizes imaging prostate tissue by using transrectal optical applicator.</li> <li>• we demonstrated numerically that DOT/FDOT measurements is less sensitive to a negative-contrast target than to a positive-contrast target, and detecting a target of negative-contrast in the trans-rectal prostate-imaging geometry is especially challenging.</li> <li>• we conducted trans-rectal ultrasound-coupled FDOT of tissue phantoms containing target of positive or negative fluorescent contrast over the background. "Negative-contrast" target is found very challenging to reconstruct.</li> </ul>					
<b>15. SUBJECT TERMS</b> Prostate cancer, zinc, diffuse optical tomography, fluorescence diffuse optical tomography.					
<b>16. SECURITY CLASSIFICATION OF:</b>			<b>17. LIMITATION OF ABSTRACT</b> UU	<b>18. NUMBER OF PAGES</b> 25	<b>19a. NAME OF RESPONSIBLE PERSON</b> USAMRMC
<b>a. REPORT</b> U	<b>b. ABSTRACT</b> U	<b>c. THIS PAGE</b> U			<b>19b. TELEPHONE NUMBER (Include area code)</b>

## TABLE OF CONTENTS

<b>1. Introduction</b>	1
<b>2. Body</b>	2
2.1 Analytical approaches to photon diffusion in trans-rectal imaging geometry	
-----	2
2.2 Numerical evaluation of photon diffusion and fluorescence measurements in response to a target of positive or negative contrast in an otherwise homogenous background	
-----	7
2.3 Experimental trans-rectal FDOT Measurement	15
<b>3. Key Research Accomplishments</b>	17
<b>4. Reportable Outcomes</b>	18
<b>5. Conclusions</b>	19
<b>References</b>	19
<b>Appendices</b>	21

## 1. INTRODUCTION

### 1.1 Objective

The long-term objective of this research is to develop an imaging technology for detecting prostate cancer based on trans-rectal fluorescence diffuse optical tomography (FDOT) of zinc-specific fluorescent marker. The specific aims of this research are to evaluate the challenges unique to trans-rectal FDOT of zinc-specific fluorescence probe, and to assess the strategies of overcoming these challenges in clinically-relevant application settings.

### 1.2 Background

Zinc is a well-established metabolic marker of prostate cancer [1]. Benign prostate tissues secrete zinc in the form of  $\text{Zn}_3\text{Citrate}_2$ , and zinc has a concentration of approximately 10mM in prostatic fluid. In cancerous prostate tissue the zinc secretion ceases, resulting in five to ten folds of reduced level of zinc in the associated prostatic fluid. It is thus hypothesized that a fluorescence reagent with the affinity to zinc will be loaded up more by the tissue containing more free zinc, and much less in cancerous prostatic tissue, generating a “reverse-uptake” of the fluorescent probe. Subsequently, a fluorescence optical imaging approach for detecting prostate cancer based on a zinc-specific fluorescent probe has to be able to recover a target (or targets) of interest that has a weaker fluorescence than the background does. Such “reverse-uptake” or “negative-contrast” case is projected to be more challenging than the conventional FDOT cases [2-12] of which the task is to reconstruct a strong fluorescence target (or targets) within a weakly-fluorescent background. This project aims to identify and characterize the challenges associated with trans-rectal FDOT of target with a “negative contrast” over the background fluorescence.

### 1.3 Specific aims

This research has the following specific aims to achieve: (A) to study algorithms to enable trans-rectal FDOT image reconstruction, and to develop methods to assess how sensitive the trans-rectal fluorescence measurement is to a “negative-contrast” fluorescence target in comparison to a positive-contrast fluorescence target; (B) to experimentally evaluate the feasibilities or challenges of trans-rectal FDOT of “negative-contrast” fluorescence; (C) to develop procedures for extracting the spatial information from imagery of trans-rectal ultrasound as the spatial constraint information to improve trans-rectal DOT/FDOT image reconstruction.

### 1.4 Overview of the progresses and trainings in year 2

The original pre-doctoral trainee PI, Mr. Guan Xu, completed his doctoral dissertation during the year 2 of this project. Dr. Xu then accepted a post-doctoral position in the University of Michigan Medical School to enhance his academic research career. Dr. Xu continues to be involved in this project, as he is revising a paper that has been “tentatively accepted” by Medical Physics at the time of this annual report being submitted. The current pre-doctoral trainee PI is Mr. Anqi Zhang. The year 2 report thus contains progresses contributed by both the former and current trainee PIs.

During the year 2 of this study, we have furthered our understanding of the challenges and feasibilities of trans-rectal FDOT of “negative-contrast” fluorescence. The progresses in year-2 include: (1) A new analytic framework is developed for quantifying photon diffusion associated with the source and the detector positioned on cylindrical medium-applicator interfaces, the interfaces that apply to both the outward-imaging geometry using a trans-rectal

applicator and the inward-imaging geometry using an external cylindrical applicator; (2) Numerical studies are conducted using analytic and finite element methods to characterize diffuse optical and diffuse fluorescence measurements to targets with positive-contrast or negative-contrast over the background medium; (3) Trans-rectal ultrasound coupled fluorescence diffuse optical tomography measurements of tissue phantoms with a target of negative or positive fluorescence contrast over the background are demonstrated.

During the year 2 of this study, the continuing trainee-PI has also enrolled in required course-work, completed animal protocol training, presented in seminars and conferences, and published journal papers.

## 2. BODY

### 2.1 Analytical approaches to photon diffusion in trans-rectal imaging geometry

#### 2.1.1 The idealized geometry for trans-rectal DOT/FDOT imaging

Trans-rectal DOT/FDOT involves a geometry wherein the tissue is being imaged outwardly using an internal optical applicator [13]. This outward-imaging geometry is different from the conventional side-way imaging geometry wherein the tissue is being imaged using a planar optical applicator [14, 15], as well as the conventional inward-imaging geometry wherein the tissue is being imaged by an external optical applicator [16, 17]. The idealizations of these three imaging geometries are illustrated in Fig. 1: in a “*concave*” geometry the photon probes the medium enclosed by a cylindrical tissue-applicator interface; in a “*convex*” geometry the photon probes the regime enclosing a cylindrical tissue-applicator interface; in a “*semi-infinite*” geometry the photon probes the medium that has a planar interface with the applicator.

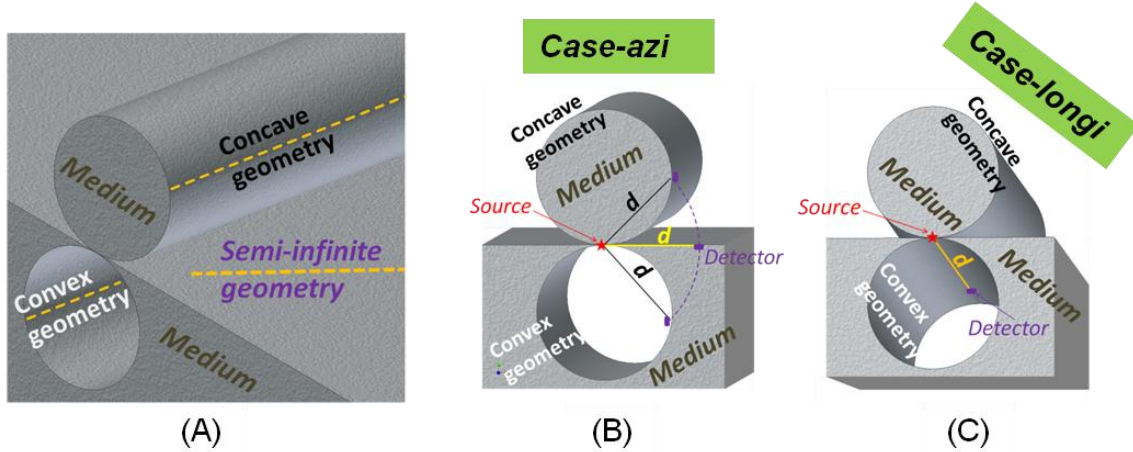


Figure 1. Three geometries of approximating the tissue-applicator interface are illustrated in (A). The geometries include a “*concave*” geometry representing the medium being enclosed by the circular cylindrical tissue-applicator interface, a “*convex*” geometry representing the medium enclosing the circular cylindrical tissue-applicator interface, and a “*semi-infinite*” geometry representing the medium interfacing with a planar applicator. For the *concave* and *convex* geometries, there are two specific directions for evaluating the photon fluence rate: a “*case-azi*” configuration shown in (B) that represents the case of having both source and detector on the same azimuthal plane, and a “*case-longi*” configuration shown in (C) that represents the case of having both source and detector on the same longitudinal line. In both (B) and (C) the line-of-sight distance between the source and the position of photon detection is denoted by  $d$ .

The behavior of photon fluence associated with the **convex** geometry, which represents the idealized trans-rectal DOT/FDOT geometry, must differ from that with the “**concave**” or “**semi-infinite**” geometry; and to our knowledge the analytical treatment of photo diffusion for such “**convex**” geometries has not been demonstrated previously. Although numerical computations using methods such as finite-element-analysis can solve photon fluence in any geometry, analytical understanding is always fundamental and may provide new insights.

Based on a novel analytical approach to photon diffusion in the **convex** geometry and “**concave**” geometry [18, 19], we gained new insights to how trans-rectal DOT/FDOT measurements are different from DOT/FDOT measurements in other geometries. By comparing the photon fluence with respect to the line-of-sight source-detector distance in the **concave**, **semi-infinite**, and **convex** geometries, respectively, the effects of the medium-applicator interfacing curvature and the dimension of the curvature to the diffuse photon measurements are better understood [20, 21, 22].

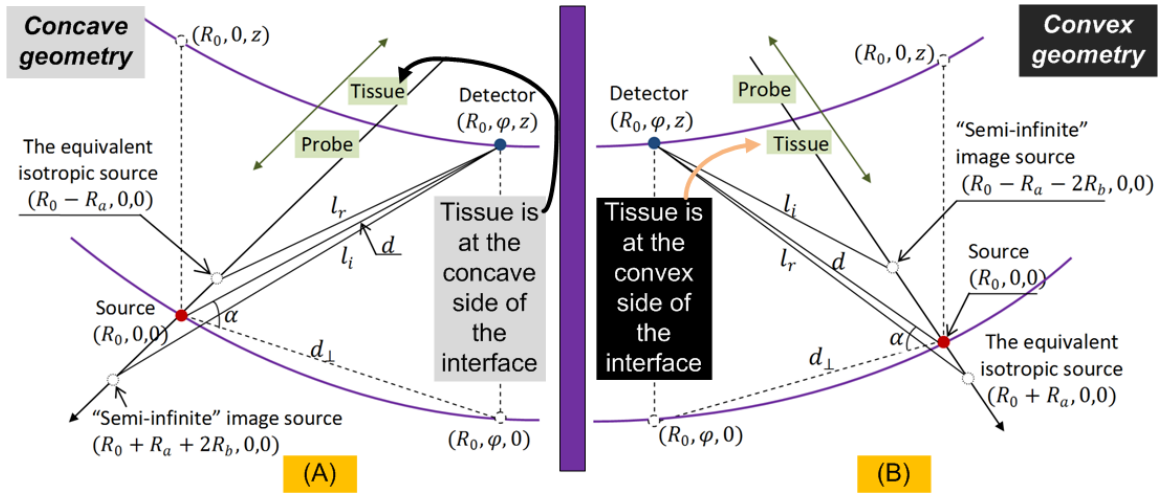


Figure 2. Notations and physical entities of **concave** and **convex** geometries. (A) The tissue is at the **concave** side of the circular cylindrical tissue-applicator interface, so the equivalent isotropic source of the physical source that illuminates into the medium is located closer to the center axis than the physical source is. (B) The tissue is at the **convex** side of the circular cylindrical tissue-applicator interface, so the equivalent isotropic source of the physical source that illuminates into the medium is located farther from the center axis than the physical source is.

### 2.1.2 Steady-state photon diffusion: “**concave**” geometry versus “**convex**” geometry

The general case of a source and a detector located on the tissue-applicator interface is illustrated in Fig. 2(A) and (B), for **concave** and **convex** geometries, respectively. The tissue enclosed by the interface in the **concave** geometry or enclosing the interface in the **convex** geometry has an absorption coefficient  $\mu_a$ , a reduced scattering coefficient  $\mu_s'$ , a diffusion coefficient  $D$ , and an effective attenuation coefficient  $k_0 = \sqrt{\mu_a/D}$ . The radius of the idealized, infinitely long circular cylindrical interface is  $R_0$ , therefore by using cylindrical coordinates, the source with an intensity of  $S$  locates at  $(R_0, 0, 0)$  and the detector locates at  $(R_0, \phi, z)$ . The line-of-sight distance between the source  $(R_0, 0, 0)$  and the detector  $(R_0, \phi, z)$  is denoted by  $d$ . The projection of  $d$  to the azimuthal plane or the projection of  $d$  perpendicular to the longitudinal axis of the cylindrical interface is denoted as  $d_\perp = d \cdot \cos \alpha$ , where  $\alpha$  is the angle between  $d$  and  $d_\perp$ . The position of the

detector with respect to the source can then be represented by  $(\alpha, d_\perp)$ . If keeping the source fixed at  $(R_0, 0, 0)$  and increasing the radius  $R_0$ , the detector will eventually reach a plane that is tangential to the shown cylindrical interface and intersects with the interface at the longitudinal line crossing the source  $(R_0, 0, 0)$ . Such a plane forms the “semi-infinite geometry” limit of the **concave** or **convex** geometry.

We have developed a new representation of the cylindrical-coordinate solutions of steady-state photon diffusion in the **concave** geometry, between a detector  $\vec{r}$  and a physical source  $\vec{r}'$  on the physical boundary as [18, 22]

$$\Psi_{conC} = \frac{S}{4\pi^2 D} \int_{-\infty}^{\infty} dk \left\{ \exp[ik(z - z')] \sum_{m=-\infty}^{\infty} I_m[k_{eff}(R_0 - R_a)] K_m(k_{eff} R_0) \right. \\ \left. \left\langle 1 - \frac{I_m(k_{eff} R_0)}{K_m(k_{eff} R_0)} \frac{K_m[k_{eff}(R_0 + R_b)]}{I_m[k_{eff}(R_0 + R_b)]} \right\rangle \exp[im(\varphi - \varphi')] \right\} \quad (1.conC)$$

where  $I_m$  and  $K_m$  are the modified Bessel functions of the 1<sup>st</sup> and the 2<sup>nd</sup> kinds, respectively,  $k_{eff} = \sqrt{k^2 + k_0^2}$ ,  $R_a = 1/\mu'_s$ ,  $R_b = 2AD$ ,  $A$  is a coefficient determined by the change of the refractive indices across the interface. Similarly, we have for the first time developed the cylindrical coordinate solutions of steady-state photon diffusion in the **convex** geometry, between a detector  $\vec{r}$  and a physical source  $\vec{r}'$  on the physical boundary as [18, 22]

$$\Psi_{conV} = \frac{S}{4\pi^2 D} \int_{-\infty}^{\infty} dk \left\{ \exp[ik(z - z')] \sum_{m=-\infty}^{\infty} I_m(k_{eff} R_0) K_m[k_{eff}(R_0 + R_a)] \right. \\ \left. \left\langle 1 - \frac{K_m(k_{eff} R_0)}{I_m(k_{eff} R_0)} \frac{I_m[k_{eff}(R_0 - R_b)]}{K_m[k_{eff}(R_0 - R_b)]} \right\rangle \exp[im(\varphi - \varphi')] \right\} \quad (1.conV)$$

### 2.1.3 Approximation to steady-state photon diffusion in “concave” and “convex” geometries with large radius: enabling qualitative comparison against semi-infinite geometry

To understand the generalized behavior of the steady-state photon diffusion versus source-detector distance in **concave** and **convex** geometries, we now consider that the radius of the **concave** or **convex** geometry is much greater than the source-detector distance that is also in the diffusion regime, i.e., we have assumed that  $R_0 \gg d \gg R_a, R_b$ .

In the **concave** geometry as shown in Fig. 2(A), we have

$$l_r = d \sqrt{1 + \frac{R_a^2}{d^2} - \frac{R_a}{R_0} (\cos \alpha)^2}; \quad l_i = d \sqrt{1 + \frac{(R_a + 2R_b)^2}{d^2} + \frac{R_a + 2R_b}{R_0} (\cos \alpha)^2} \quad (2.conC)$$

then Eqs. (1.conC) can be simplified to [21]

$$\Psi_{conC} = \frac{S}{2\pi D} \frac{1}{d^2} \exp \left\{ - \left[ k_0 d + \frac{d}{2k_0 R_b (R_0 - R_a)} - \frac{2R_0 - R_a + 2R_b}{4R_0 R_b (R_0 - R_a)} (\cos \alpha)^2 d^2 \right] \right\} \exp \left[ \frac{(R_0 + 2R_b)^2}{4R_b (R_0 - R_a)} \right] [k_0 R_b (R_a + R_b)] \quad (3.conC)$$

In the convex geometry as shown in Fig. 2(B), we have

$$l_r = d \sqrt{1 + \frac{R_a^2}{d^2} + \frac{R_a}{R_0} (\cos \alpha)^2}; \quad l_i = d \sqrt{1 + \frac{(R_a + 2R_b)^2}{d^2} - \frac{R_a + 2R_b}{R_0} (\cos \alpha)^2} \quad (2.conV)$$

then Eqs. (1.conV) can be simplified to [21]

$$\Psi_{conv} = \frac{S}{2\pi D} \frac{1}{d^2} \exp \left\{ - \left[ k_0 d - \frac{d}{2k_0 R_b (R_0 + R_a)} + \frac{2R_0 + R_a - 2R_b}{4R_0 R_b (R_0 + R_a)} (\cos \alpha)^2 d^2 \right] \right\} \exp \left[ - \frac{(R_0 + 2R_b)^2}{4R_b (R_0 + R_a)} \right] [k_0 R_b (R_a + R_b)] \quad (3.conV)$$

In comparison, in semi-infinite geometry [15]

$$\Psi_{semi} = \frac{S}{2\pi D} \frac{1}{d^2} \exp \{ -k_0 d \} [k_0 R_b (R_a + R_b)] \quad (3.semi)$$

#### 2.1.4 The change of steady-state photon fluence with respect to $d$ for large radius cases

Equation (3.semi) indicates that on a semi-infinite interface,  $\ln(\Psi_{semi} d^2)$  decreases versus  $d$  at a rate of  $k_0$ , i.e.

$$\frac{\partial \ln(\Psi_{semi} d^2)}{\partial d} = -k_0 \quad (4.semi)$$

On a **concave** interface of larger radius, Eq. (3.conC) indicates  $\ln(\Psi_{conC} d^2)$  reducing versus  $d$  as

$$\frac{\partial \ln(\Psi_{conC} d^2)}{\partial d} = - \left\{ k_0 + \frac{1}{2k_0 R_b (R_0 - R_a)} - \left[ \frac{2R_0 - R_a + 2R_b}{2R_0 R_b (R_0 - R_a)} \right] \cos \alpha d_{\perp} \right\} \quad (4.conC)$$

where  $d_{\perp} = d \cos \alpha$  is the projection of  $d$  to the azimuthal plane. Along the longitudinal direction, termed *case-longi*, i.e.,  $\cos \alpha = 0$ , we have [21, 22]

$$\left. \frac{\partial \ln(\Psi_{conC} d^2)}{\partial d} \right|_{longi} = - \left[ k_0 + \frac{1}{2k_0 R_b (R_0 - R_a)} \right] \quad (4.conC.longi)$$

Equation (4.conC.longi) indicates that when the source and detector are positioned only along the longitudinal direction,  $\ln(\Psi_{conC} d^2)$  reduces versus  $d$  at a rate greater than  $k_0$ . Along the azimuthal direction, termed *case-azi*, i.e.,  $\cos \alpha = 1$ ,  $d_{\perp} = d$ , we have [21, 22]

$$\left. \frac{\partial \ln(\Psi_{conC} d^2)}{\partial d} \right|_{azi} = - \left\{ k_0 + \frac{1}{2k_0 R_b (R_0 - R_a)} - \left[ \frac{2R_0 - R_a + 2R_b}{2R_0 R_b (R_0 - R_a)} \right] d \right\} \quad (4.conC.azi)$$

It can be demonstrated that the rate of the reduction of  $\ln(\Psi_{conC} d^2)$  in Eq. (4.conC.azi) versus  $d$  is actually smaller than  $k_0$ .

On a **convex** interface with large radius, Eq. (3.conV) indicates  $\ln(\Psi_{conV} d^2)$  reducing versus  $d$  as [21, 22]

$$\frac{\partial \ln(\Psi_{conV} d^2)}{\partial d} = - \left\{ k_0 - \frac{1}{2k_0 R_b (R_0 + R_a)} + \left[ \frac{2R_0 + R_a - 2R_b}{2R_0 R_b (R_0 + R_a)} \right] \cos \alpha d_{\perp} \right\} \quad (4.conV)$$

Along the longitudinal direction as in *case-longi*, i.e.,  $\cos \alpha = 0$ , we have

$$\left. \frac{\partial \ln(\Psi_{conV} d^2)}{\partial d} \right|_{longi} = - \left[ k_0 - \frac{1}{2k_0 R_b (R_0 + R_a)} \right] \quad (4.conV.longi)$$

Equation (4.conV.longi) indicates that when the source and detector are positioned only along the longitudinal direction,  $\ln(\Psi_{conV} d^2)$  reduces versus  $d$  at a rate smaller than  $k_0$ . Along the azimuthal direction as in *case-azi*, i.e.,  $\cos \alpha = 1$ ,  $d_{\perp} = d$ , we have



$$\left. \frac{\partial \ln(\Psi_{conV} d^2)}{\partial d} \right|_{azi} = - \left\{ k_0 - \frac{1}{2k_0 R_b (R_0 + R_a)} + \left[ \frac{2R_0 + R_a - 2R_b}{2R_0 R_b (R_0 + R_a)} \right] d \right\} \quad (4.conV.azi)$$

It can be demonstrated that the rate of the reduction of  $\ln(\Psi_{conV} d^2)$  in Eq. (4.conV.azi) versus  $d$  is actually greater than  $k_0$ .

### 2.1.5 A set of spiral-paths with interesting characteristics in terms of steady-state diffusion

We also have from Eq. (4.conC) that when the source and detector are positioned along a set of spiral paths defined by the following relationship [20, 21]

$$\cos \alpha_{conC} = \frac{1}{k_0 d_{\perp}} \frac{R_0}{2R_0 - R_a + 2R_b} \quad (4.conC.spiral)$$

$\ln(\Psi_{conC} d^2)$  reduces versus  $d$  at a rate of  $k_0$ , i.e., identical to the rate when evaluated along a straight-line on a semi-infinite medium-applicator interface.

We also have from Eq. (4.conV) that when the source and detector are positioned along a set of spiral paths defined by the following relationship [20, 21]

$$\cos \alpha_{conV} = \frac{1}{k_0 d_{\perp}} \frac{R_0}{2R_0 + R_a - 2R_b} \quad (4.conV.spiral),$$

$\ln(\Psi_{conV} d^2)$  reduces versus  $d$  at a rate of  $k_0$ , i.e., identical to the rate when evaluated along a straight-line on a semi-infinite medium-applicator interface.

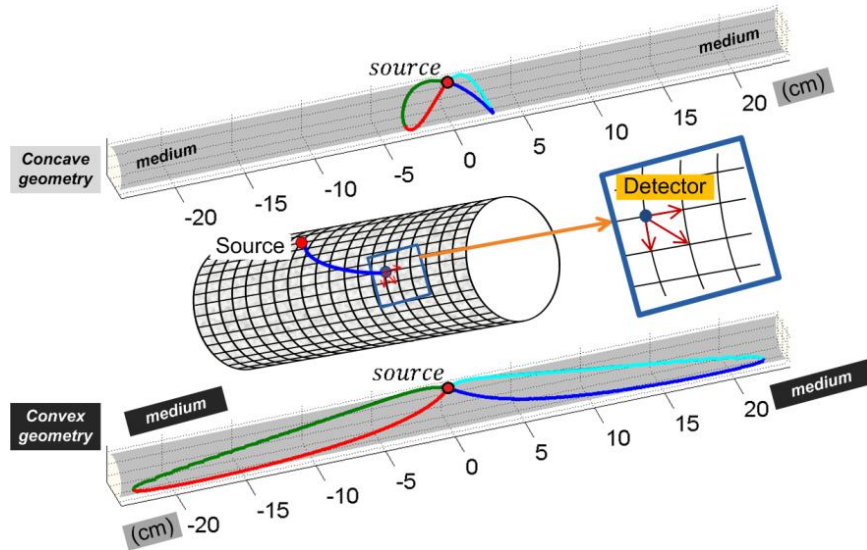


Figure 3. Spiral paths for **concave** and **convex** geometries of centimeter-order radii are calculated based on analytic results derived in Eqs. (1.conC) and (1.conV). For a fixed source, a detector has three directions to move away from the source: along the azimuthal direction, along the longitudinal direction, and along the diagonal of the above two directions. For each possible future location of the detector, the photon fluence rate at that position is compared with the case in the semi-infinite geometry for the same line-of-sight distance of the detector from the source, and the position with the least difference in the evaluated photon fluence rate is the next starting position of the detector. The shown complete sets of the spiral profile for **concave** geometry (upper) and **convex** geometry (lower) are computed for a cylinder radius of  $R_0 = 1.5\text{cm}$  and optical properties of  $\mu_a = 0.02\text{cm}^{-1}$ ,  $\mu'_s = 5\text{cm}^{-1}$  and  $A = 1.86$ .

Equations (4.conC.spiral) and (4.conV.spiral) demonstrate that in **concave** or **convex** geometries of large radius there are spiral-paths along which the decay rate of photon fluence is identical to that along a straight line on a semi-infinite interface for the same line-of-sight source-detector distance. The existence of such spiral-paths for **concave** or **convex** geometry of smaller radial dimension is found numerically [21], as summarized in Fig. 3. In both **concave** and **convex** geometries, the spiral-paths have two lobes symmetric to the source location, and each lobe is symmetric with respect to a middle sagittal plane containing the source. The spiral-paths are shown to contain four identical quadrants. Monte-Carlo (MC) and Finite-element-method (FEM) solution of photon diffusion confirmed that the decay-rate of photon fluence along the spiral paths was indeed equal to that along a straight-line on a semi-infinite interface.

## 2.2 Numerical evaluation of photon diffusion and fluorescence measurements in response to a target of positive or negative contrast in an otherwise homogeneous background

### 2.2.1 Change to diffuse photon measurement by a strong target of positive or negative contrast aligned azimuthally with the spiral paths---- evaluation based on finite element method [21]

FEM computation based on NIRFAST [23] is implemented to evaluate the photon fluence along the spiral-paths when a strong anomaly resides in the medium. We choose to evaluate the changes to photon diffusion along the spiral-paths, since these paths make it convenient to compare among **concave**, **convex**, and semi-infinite geometries, and the results will show how sensitive the diffuse photon measurement is to negative-contrast target versus positive-contrast target for the same level of contrast.

The FEM meshing domain is illustrated in Fig. 4 (A), (B), and (C) for **concave**, semi-infinite, and **convex** geometries, respectively. In the **concave** geometry, the meshing volume is 14cm in height and 1.5cm in radius, which is discretized into 76,620 nodes and 349,697 tetrahedral elements. In the semi-infinite geometry, the meshing volume is a rectangle of  $15 \times 11 \times 5.5 \text{ cm}^3$ , which is discretized into 88,941 nodes and 496,211 elements. In the **convex** geometry, the meshing domain is the volume between two concentric cylinders of 15cm in height, with 1.5cm inner radius and 6cm outer radius. The meshing volume is discretized into 83,312 nodes and 437,039 tetrahedral elements.

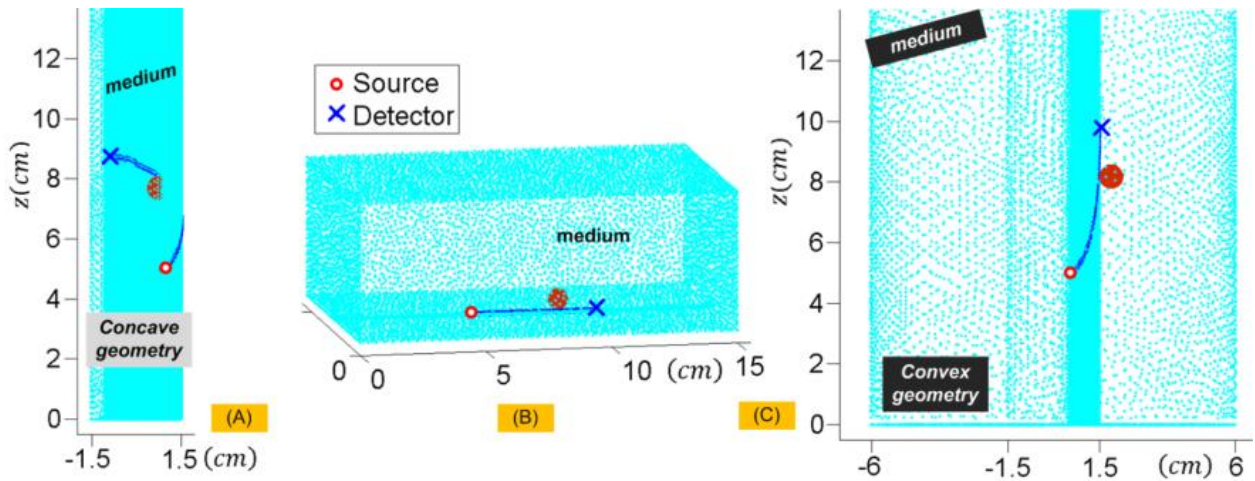


Figure 4. Finite-element discretization of the imaging domain and the position of the anomaly with strong perturbation strength. (A) **concave** geometry, (B) semi-infinite geometry, and (C) **convex** geometry.

We consider a spherical anomaly of 0.4cm in radius and 0.5cm in depth that is aligned azimuthally with one quadrant of the spiral-paths or the straight line in the three geometries. Table 1 lists the four sets of optical parameters assigned to the single anomaly, which include **4:1 positive  $\mu_a$ , 1:4 negative  $\mu_a$ , 2:1 positive  $\mu'_s$ , and 1:2 negative  $\mu'_s$  contrasts** over the background medium. The results of FEM simulation based on the four cases of contrasts as specified in Table 1 are given in Fig. 5. In each of the sub figures from (A) to (D), the photon fluence rates are compared among four configurations. At the macroscopic scale of near-5cm range for  $d$ , the photon fluence curves for the three geometries with the anomaly are distinguished from the green reference except for negative  $\mu_a$  contrast; however the photon fluence curves for the three geometries with the anomaly are nearly indistinguishable. At the microscopic level shown as the insets in Fig. 5, the photon fluence curves of the **concave** and **convex** geometries are very close to and at the opposite sides of the curve of semi-infinite geometry, for anomaly of either absorption or scattering contrast. The measurement is less sensitive to a **negative absorption contrast** than to a **positive absorption contrast**.

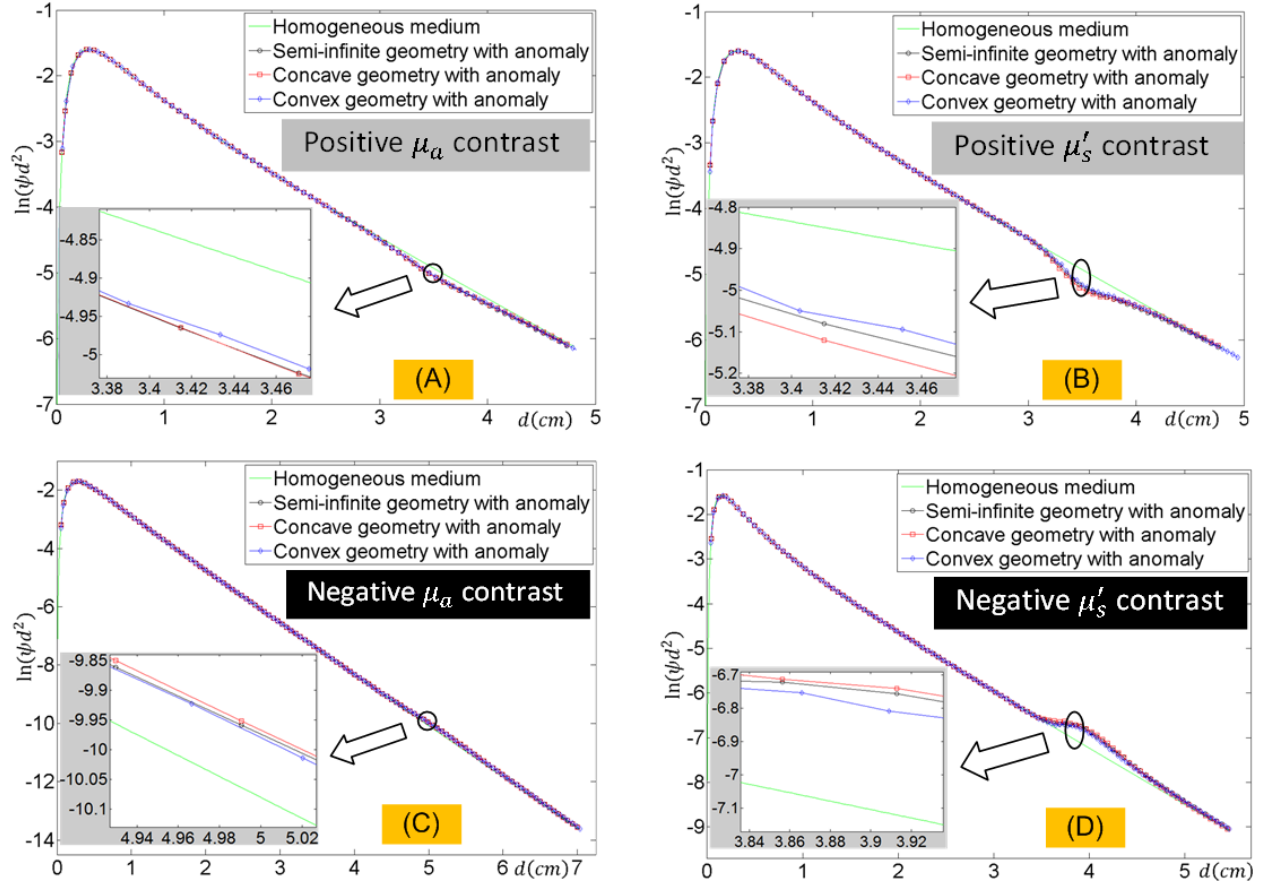


Figure 5. Photon fluence when one strong anomaly resides in the otherwise homogeneous background medium. The anomaly possesses (A) positive  $\mu_a$  contrast, (B) positive  $\mu'_s$  contrast, (C) negative  $\mu_a$  contrast, and (D) negative  $\mu'_s$  contrast over the background.

The shown curves of photon fluence are plotted for (1) along a straight line in semi-infinite geometry of homogenous medium, (2) along a straight line in semi-infinite geometry having the anomaly aligned with the straight line, (3) along the spiral profile in **concave** geometry having the anomaly aligned with the spiral profile, and (4) along the spiral profile in **convex** geometry having the anomaly aligned with the spiral profile.

Table 1. Optical parameters used for evaluating the change to photon fluence rate by an anomaly

		Background $\mu_a$ ( $\text{cm}^{-1}$ )	Background $\mu'_s$ ( $\text{cm}^{-1}$ )	Anomaly $\mu_a$ ( $\text{cm}^{-1}$ )	Anomaly $\mu'_s$ ( $\text{cm}^{-1}$ )
Set 1	positive $\mu_a$ contrast	0.025	10.0	0.1	10.0
Set 2	positive $\mu'_s$ contrast	0.025	10.0	0.025	20.0
Set 3	negative $\mu_a$ contrast	0.1	10.0	0.025	10.0
Set 4	negative $\mu'_s$ contrast	0.025	20.0	0.025	10.0

### 2.2.2 Steady-state fluorescence measurement with a homogeneous distribution of fluorophore

A homogeneous distribution of the fluorophore within the medium resembles the idealized situation when the normal prostatic tissue has the uptake of the zinc-specific fluorescence probe. We thus have used FEM to numerically examine the steady-state fluorescence measurement for the medium containing homogeneous distribution of the fluorophore, and compared the steady-state fluorescence among *concave* geometry, semi-infinite geometry, and *convex* geometry. The numerical examinations are performed for 5 configurations: longitudinally aligned source-detector pair on the concave interface, azimuthally aligned source-detector pair on the concave interface, source-detector pair on the semi-infinite interface, longitudinally aligned source-detector pair on the convex interface, and azimuthally aligned source-detector pair on the convex interface.

The simulation results of the fluence at the emission wavelength are illustrated in Fig. 6. The radius of the cylindrical applicator for both *concave* and *convex* geometries is  $R = 2 \text{ cm}$ . We denote  $\mu_{ax}$  and  $\mu'_{sx}$  as the absorption coefficient and reduced scattering coefficient at excitation wavelength,  $\mu_{aem}$  and  $\mu'_{sem}$  as those at emission wavelength,  $\mu_{afl}$  as the absorption coefficient of the fluorophore at the excitation wavelength,  $\eta$  as the quantum yielding efficiency of the fluorophore. These parameters chosen for the simulations are  $\mu_{ax} = 0.025 \text{ cm}^{-1}$ ,  $\mu_{aem} = 0.025 \text{ cm}^{-1}$ ,  $\mu'_{sx} = 10 \text{ cm}^{-1}$ ,  $\mu'_{sem} = 10 \text{ cm}^{-1}$ ,  $\mu_{afl} = 0.05 \text{ cm}^{-1}$  and  $\eta = 0.1$ . We therefore have made some approximations, such as neglecting the wavelength-dependence of the scattering and the re-excitation/emission effect.

As can be seen in Fig. 6, the decay of the emission-fluence in either *concave* or *convex* geometry follows the same trends as shown to the fluence at the excitation wavelength [18, 19], approximated by Eqs. (4.conC.longi), (4.conC.azi), (4.conV.longi), and (4.conV.azi). Specifically, in *concave* geometry, the emission-fluence decays slower in case-azi and faster in case-longi when comparing to that in the semi-infinite geometry for the same line-of-sight distance. In *convex* geometry, the emission-fluence decays faster in case-azi and slower in case-longi when comparing to that in the semi-infinite geometry for the same line-of-sight distance. The normalized Born ratio (i.e., the ratio of the fluence at the emission wavelength over the fluence at the excitation wavelength, both measured by the same detector) corresponding to Fig. 6 is shown in Fig. 7. It is known that the Born ratio increases with the source-detector distance. It is shown in Fig. 7 that the Born ratio is smaller in *concave* geometry and greater in *convex* geometry, in both case-azi and case-longi cases, when comparing to that in the semi-infinite geometry for the same line-of-sight distance, and the greater the source-detector separation, the

greater the difference of the Born ratio of the concave or convex from the semi-infinite geometry.

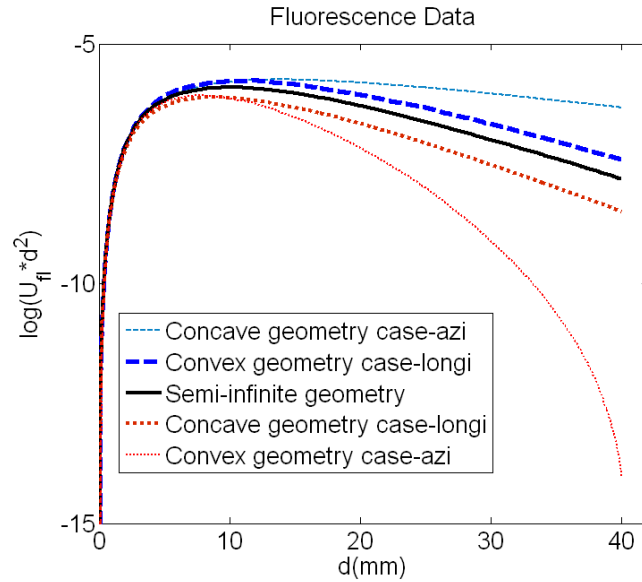


Figure 6. The photon fluence rate at the emission wavelength in the **concave** geometry and **convex** geometry with a homogeneous distribution of the fluorophore. The photon fluence at the emission wavelength decays slower in case-azi and faster in case-longi of concave geometry, when comparing to that in the semi-infinite geometry for the same line-of-sight source-detector distance. The photon fluence at the emission wavelength decays faster in case-azi and slower in case-longi of convex geometry, when comparing to that in the semi-infinite geometry for the same line-of-sight source-detector distance.

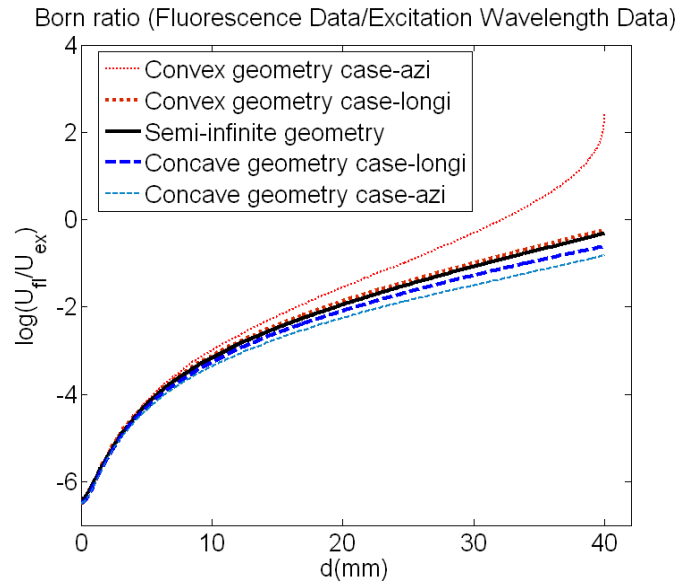


Figure 7. The changes of normalized Born ratio versus source-detector distance in the concave geometry and convex geometry with a homogeneous distribution of the fluorophore. The Born ratio is smaller in both case-azi and case-longi of concave geometry and greater in both case-azi and case-longi of convex geometry than that along a straight line on the semi-infinite interface, for the same line-of-sight source-detector distance.



### 2.2.3 Change to steady-state fluorescence measurement by a target of positive or negative contrast with respect to otherwise homogeneous distribution of fluorophore

We also studied the changes to steady-state fluence at the emission wavelength as well as the Born ratio when the otherwise homogeneous medium contains a target of fluorescence contrast, either positive or negative, over the background. We consider the following simplified configurations of the fluorescence target with respect to the source-detector positions: (1) the fluorescence target and the source-detector pair are all at the same **azimuthal** plane of a **concave** geometry with the source and the detector symmetric to the target; (2) the fluorescence target and the source-detector pair are all at the same **azimuthal** plane of a **convex** geometry with the source and the detector symmetric to the target; (3) the fluorescence target and the source-detector pair are all at the same **sagittal** plane of a **concave** geometry with the source and the detector symmetric to the target; (4) the fluorescence target and the source-detector pair are all at the same **sagittal** plane of a **convex** geometry with the source and the detector symmetric to the target; and (5) to which these four configurations are compared against, wherein the fluorescence target and the source-detector pair are all at the same **normal** plane of a **semi-infinite** geometry with the source and the detector symmetric to the target.

The FEM meshes of (1) and (2) are illustrated with respect to (5) in Fig. 8, and those of (3) and (4) are illustrated with respect to (5) in Fig. 9. In all these cases, the anomaly of fluorescence is set as a sphere with a radius of 6mm, and the center of the anomaly is placed 7mm away from the applicator interface. The radius of the cylindrical applicator is  $R = 2\text{ cm}$ . The background optical parameters are  $\mu_{ax} = 0.025\text{ cm}^{-1}$ ,  $\mu_{aem} = 0.025\text{ cm}^{-1}$ ,  $\mu'_{sx} = 10\text{ cm}^{-1}$  and  $\mu'_{sem} = 10\text{ cm}^{-1}$ . For an anomaly with a **2:1 positive contrast** over the background, the absorption coefficient of it at the excitation wavelength is  $\mu_{afl\_anomaly} = 0.1\text{ cm}^{-1}$  and that of the background fluorophore is  $\mu_{afl\_background} = 0.05\text{ cm}^{-1}$ . The fluorescence yield is  $\eta = 0.1$ . For an anomaly with a **1:2 negative contrast** over the background, the absorption coefficient of it at the excitation wavelength is  $\mu_{afl\_anomaly} = 0.05\text{ cm}^{-1}$  and that of the background fluorophore is  $\mu_{afl\_background} = 0.1\text{ cm}^{-1}$ . The fluorescence yield is  $\eta = 0.1$ . These optical parameters for both case-azi and case-longi are summarized in Table 2.

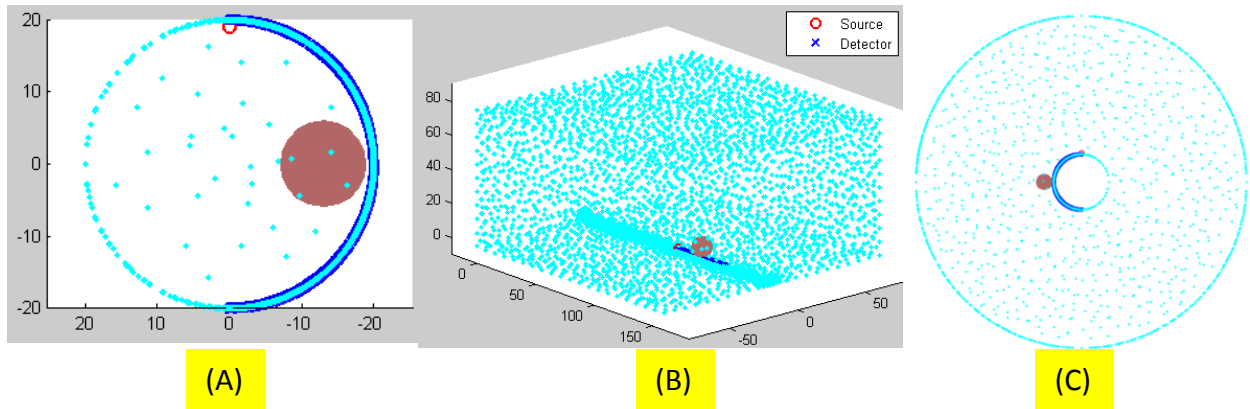


Figure 8. FEM imaging volume for case-azi. Detectors are aligned along the azimuthal plane on the applicator's interface. (A) **concave** geometry, (B) semi-infinite geometry, (C) **convex** geometry.

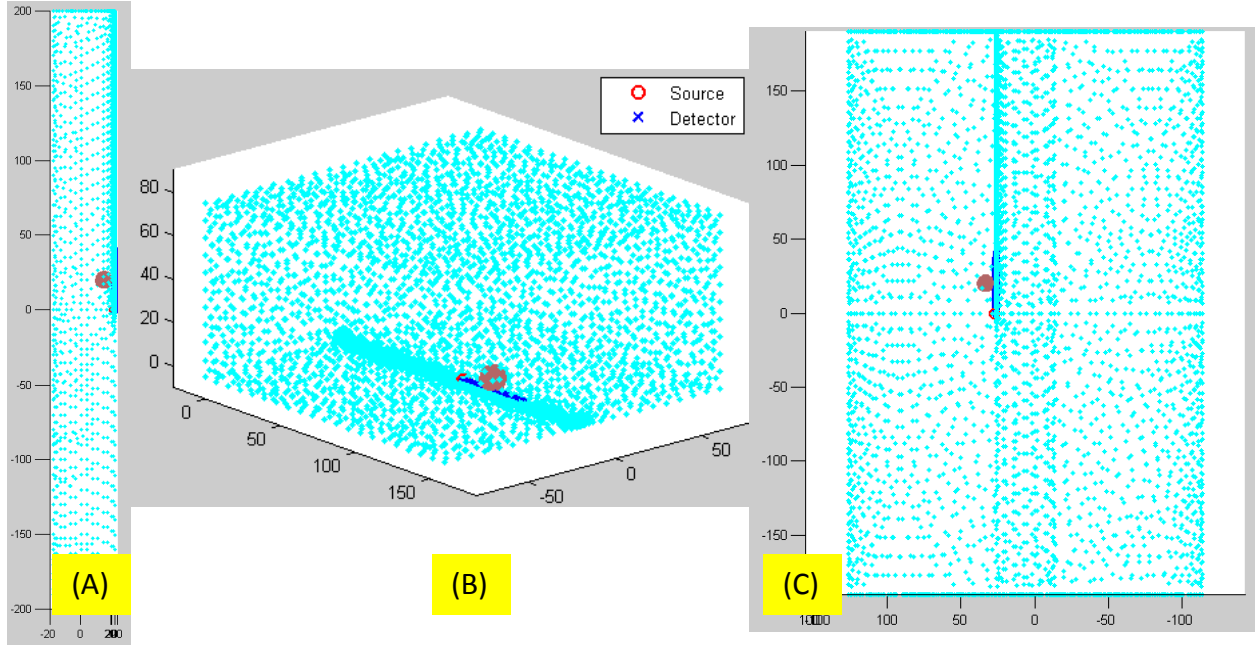


Figure 9. FEM imaging volume for case-longi. Detectors are aligned longitudinally with same azimuthal angle on the applicator's interface. (A) *concave* geometry, (B) semi-infinite geometry, (C) *convex* geometry.

Table 2. Optical parameters used for evaluating the change to florescent measurement by an anomaly

			background fluorescence $\mu_{afl\_background} (cm^{-1})$	anomaly fluorescence $\mu_{afl\_anomaly} (cm^{-1})$
Set 1	positive contrast	Case-azi	<b>0.05</b>	<b>0.1</b>
Set 2	negative contrast	Case-azi	<b>0.1</b>	<b>0.05</b>
Set 3	positive contrast	Case-longi	<b>0.05</b>	<b>0.1</b>
Set 4	negative contrast	Case-longi	<b>0.1</b>	<b>0.05</b>

The simulation results for case-azi of both *concave* and *convex* geometries are illustrated in Fig. 10 (A)-(D) as following: (A) shows the emission-fluence at the positive-contrast case, (B) is the Born ratio correspondence of (A), (C) shows the emission-fluence at the negative-contrast case, (D) is the Born ratio correspondence of (C). Figure 11 is the case-longi counterpart of Fig. 10. In all sub-plots of Figs. 10 and 11, the results corresponding to the anomaly (plotted by solid lines) are compared to the cases without the anomaly (plotted by dashed lines), to show the changes to the emission-fluence by the introduction of the target at the set parameters to the medium that originally contained a homogeneous distribution of the fluorophore.

Figure 10 demonstrates that fluorescence measurement along the azimuthal direction is significantly more challenging in the convex geometry than in the concave geometry. Figure 11 demonstrates that fluorescence measurement along the longitudinal direction is slightly more challenging in the convex geometry than in the concave geometry. Both figures show that a negative-contrast target is much more challenging to detect, regardless of the concave or convex

geometry and the case-azi or case-longi configuration. Therefore, we can anticipate that, *trans-rectal FDOT of negative-contrast target faces the lowest signal sensitivity to the introduction of the same target property.*

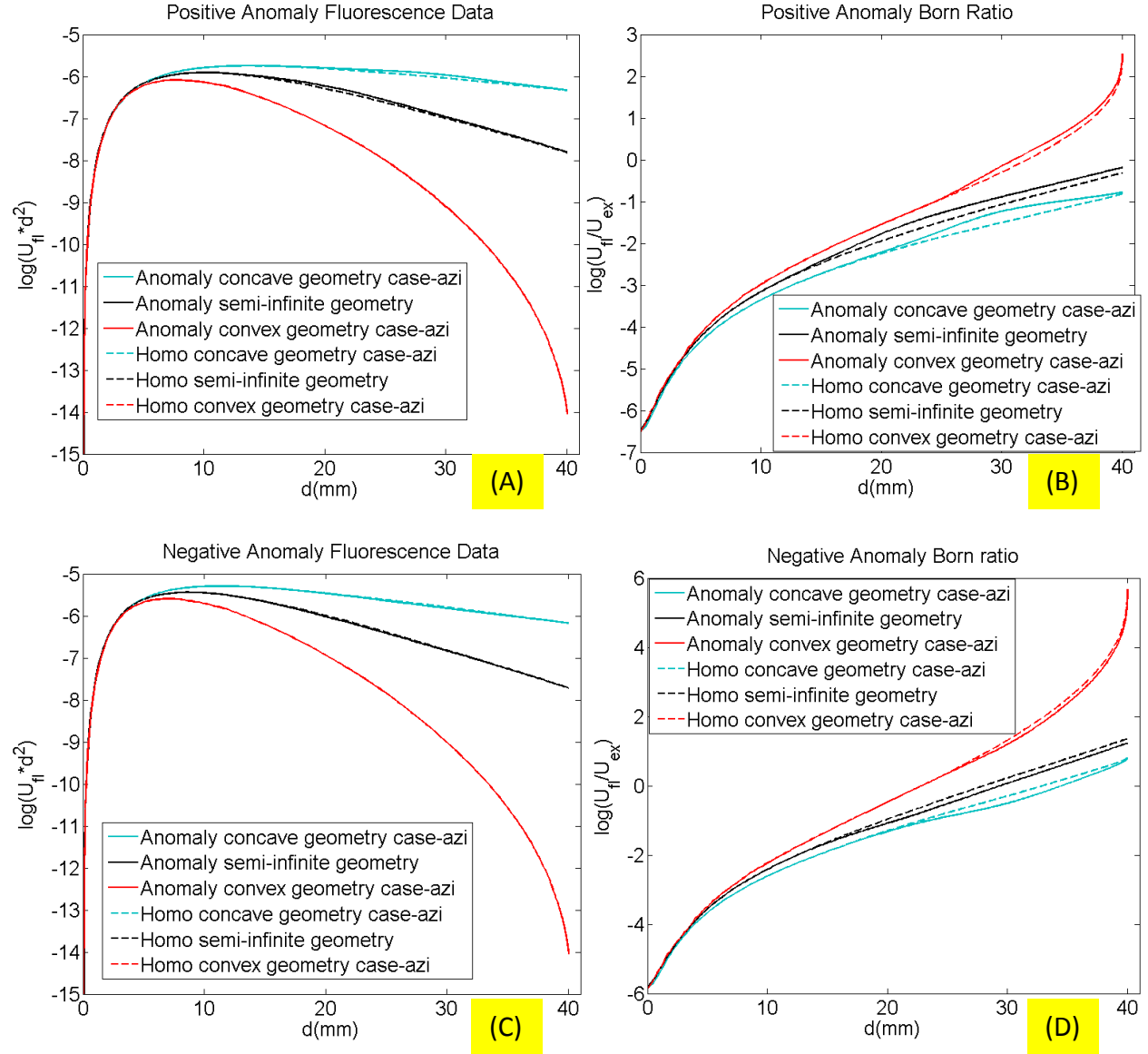


Figure 10. The comparisons of the change of fluorescent measurement due to an anomaly with fluorescence contrast in **concave**, **convex** and semi-infinite geometry in case-azi configuration. (A) The change in the fluorescence measurement due to a positive contrast anomaly. (B) The change in the Born ratio due to a positive contrast anomaly. (C) The change in fluorescence measurement due to a negative contrast anomaly. (D) The change in the Born ratio due to a negative contrast anomaly. It is indicated that the fluorescent measurement is less sensitive to negative contrast anomaly than to positive contrast anomaly and the Born ratio is more sensitive to the anomaly inclusion than the fluorescent-only measurement is.



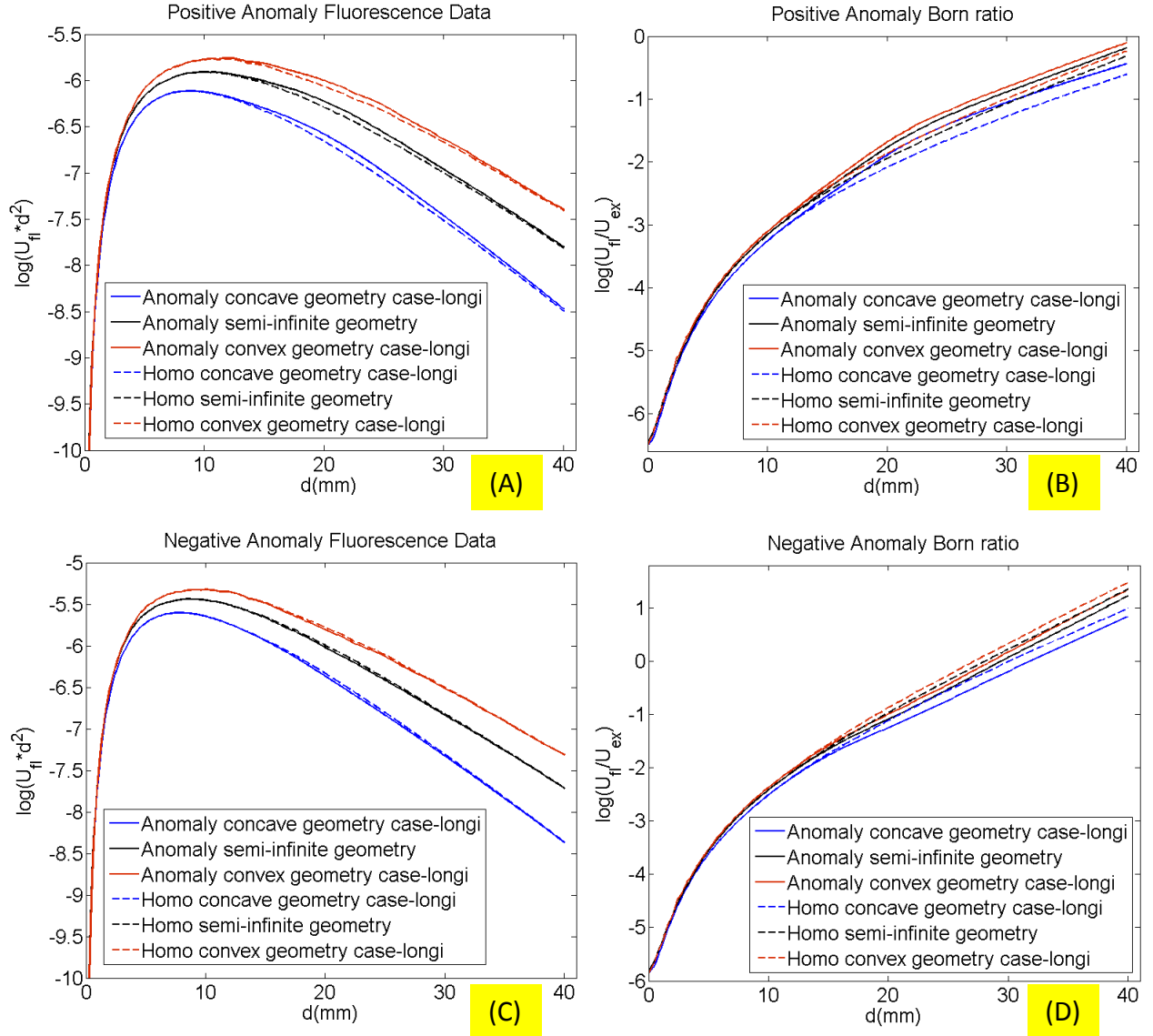


Figure 11. The comparisons of the change of fluorescent measurement due to an anomaly with fluorescence contrast in **concave**, **convex** and semi-infinite geometry in case-longi configuration. (A) The change in fluorescence measurement due to a positive contrast anomaly. (B) The change in the Born ratio due to a positive contrast anomaly. (C) The change in fluorescence measurement due to a negative contrast anomaly. (D) The change in the Born ratio due to a negative contrast anomaly. It is indicated that the fluorescent measurement is less sensitive to negative contrast anomaly than to positive contrast anomaly and the Born ratio is more sensitive to the anomaly inclusion than the fluorescent-only measurement is.

## 2.3 Experimental trans-rectal FDOT Measurement

### 2.3.1 Transrectal ultrasound-coupled FDOT system

The previous numerical analyses have clearly indicated that we should not become very optimistic about the outcome of reconstructing a target of negative contrast over the background fluorescence, particularly in trans-rectal geometry. To examine the feasibility of trans-rectal FDOT of negative-contrast target, we modified our trans-rectal ultrasound (TRUS)-coupled near-infrared (NIR) DOT system [24] for FDOT measurement. The NIR applicator coupled to TRUS transducer has 7 source channels and 7 detector channels. However, one detector channel within the applicator was out of order, likely due to aged adhesive that de-coupled or misaligned the micro-optics, leaving only 6 working channels for the detection of light from the tissue.

In terms of the system modification, as schematically shown in Fig. 12, an excitation laser diode at 705nm is coupled sequentially into the seven source channels through a fiber switch system. This 705nm laser diode is used to excite the indocyanine green (ICG) in the following phantom experiments to facilitate the measurement of the emission signals using the spectrometer of the system. For light excitation at each source channel, the six detector channels transmit the remitted signal at both the excitation (at 705nm) and the emission (centered at 785nm) to the spectrometer. The detection using a spectrometer allows separating the emission band from the excitation wavelength without a filtering scheme, for acquisition by a CCD, as long as the excitation wavelength has minimal overlapping with the emission spectra of ICG. Longer excitation wavelength (i.e., around 760nm) may be used to more effectively excite the fluorescence of ICG, however, the need to use a long-pass filter to block the excitation wavelength compromises the total emission power of the ICG. The horizontally differentiated excitation and the emission signals for the vertically separated six detector channels are shown in Fig. 13. The data acquisition time was 7 seconds.

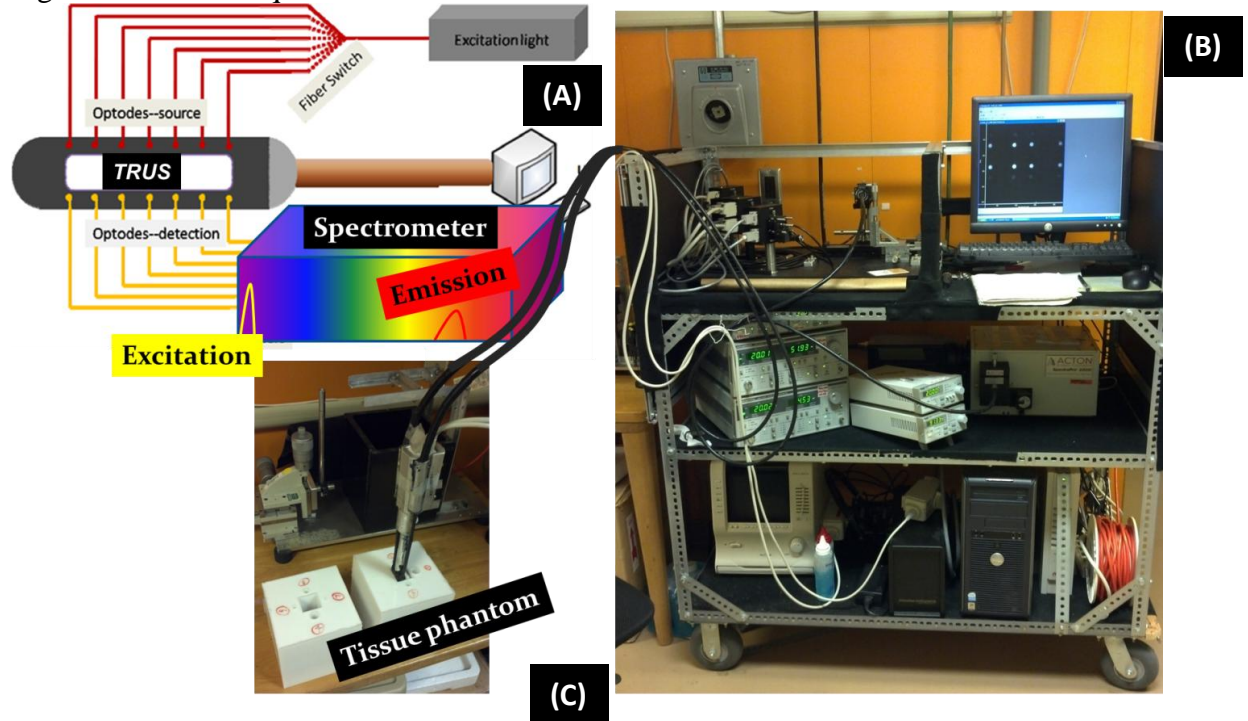


Figure 12. TRUS-coupled FDOT system. (A) System configuration. (B) The photograph of the system. (C) The applicator placed in a tissue phantom for positive-contrast test.

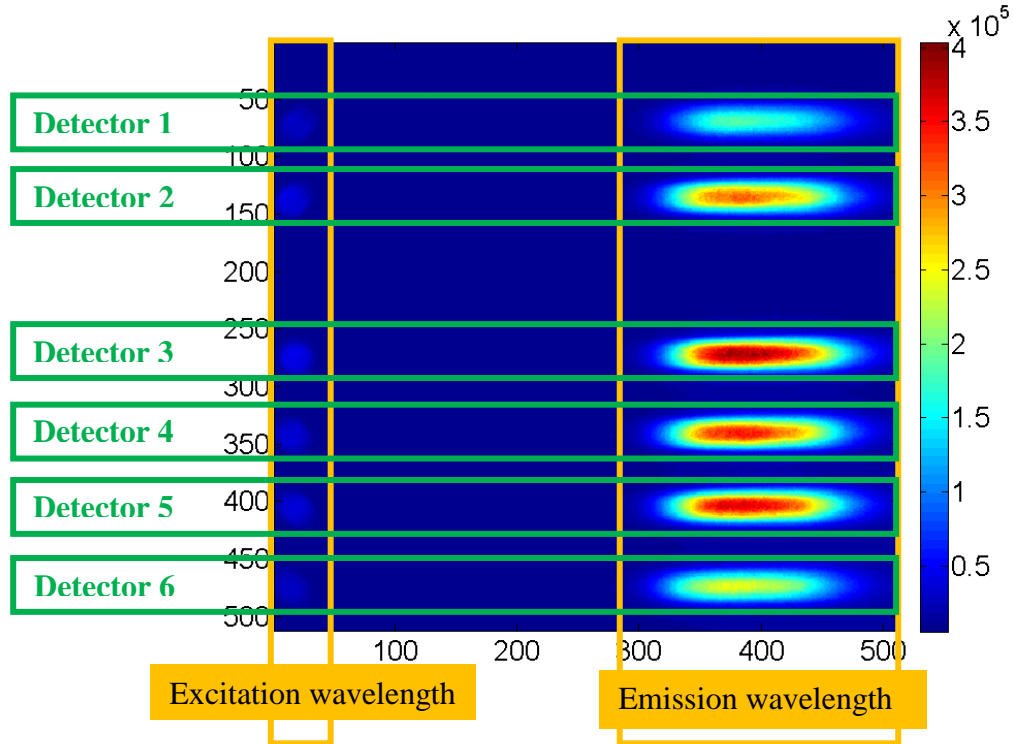


Figure 13. One typical CCD image. The data column at the left corresponds to the excitation signal, and the data column at the right corresponds to the measurement at the emission wavelength. The six rows represent the six detector channels.

### 2.3.2 TRUS-coupled FDOT of phantoms with a positive-contrast or negative-contrast target

We originally expected to take use of fluorophore with zinc-specificity that is to be developed by Andro-Diagnostics Inc in Galveston, TX in their independent project. Due to the delay in the development of the zinc-specific fluorophore, we decided to use ICG as the fluorescence probe. In regards to the main objective of this project, what to be assessed is how challenging it is to recover a negative-contrast target in a trans-rectal FDOT measurement geometry, and ICG serves the specific needs of manipulating tissue phantoms containing positive-contrast or negative-contrast fluorescence target for trans-rectal FDOT measurements.

To simulate a target with positive-contrast of fluorescence over the background, we utilized silicon-based tissue phantoms (a collaborative development [25]), the ones photographed in Fig. 12. The fluorescence target was a cylinder (1.4cm in diameter and approximately 4cm in length) filled with ICG concentration of 8  $\mu\text{M}$ , which was embedded in the non-fluorescent homogeneous background enclosing the TRUS-coupled FDOT applicator, and was 3mm away from the optical probe and in the middle-sagittal plane. To simulate a target with negative contrast of fluorescence over the background, we developed a liquid phantom with a background ICG concentration of 8  $\mu\text{M}$ , and embedded a non-fluorescent solid cylindrical phantom (1.5cm in diameter and 2.5cm in length), placed 5mm away from the optical probe and orthogonal to the middle-sagittal plane. The center locations of the targets at the two experiments were similar, as illustrated by the TRUS image of Fig. 14. The image was shown upward from the TRUS-NIR applicator, i.e., the position of the applicator was at the lower edge of the shown TRUS image.

The two sets of experiments, as one placed a target of fluorescence over a background of no-fluorescence, and the other embedded a target of no-fluorescence within a background of fluorescence, represent virtually the best-scenario cases in terms of the target-to-background contrast. The two cases, though not comprehensive, should reveal the potential of using trans-rectal FDOT to reconstruct a positive-contrast target or a negative-contrast target. It can be observed from the reconstructed results shown in Fig. 14 that, the contrast and size of the positive-contrast target were much more realistically recovered than those of the negative-contrast target. The negative-contrast target was ambiguous within a background of fluorescence that was strongly heterogeneous. The shown difficulty of recovering a target with strongly negative-contrast of fluorescence agrees with the numerical analyses in terms of the sensitivity of FDOT measurement to the target with a positive or negative contrast to the background.

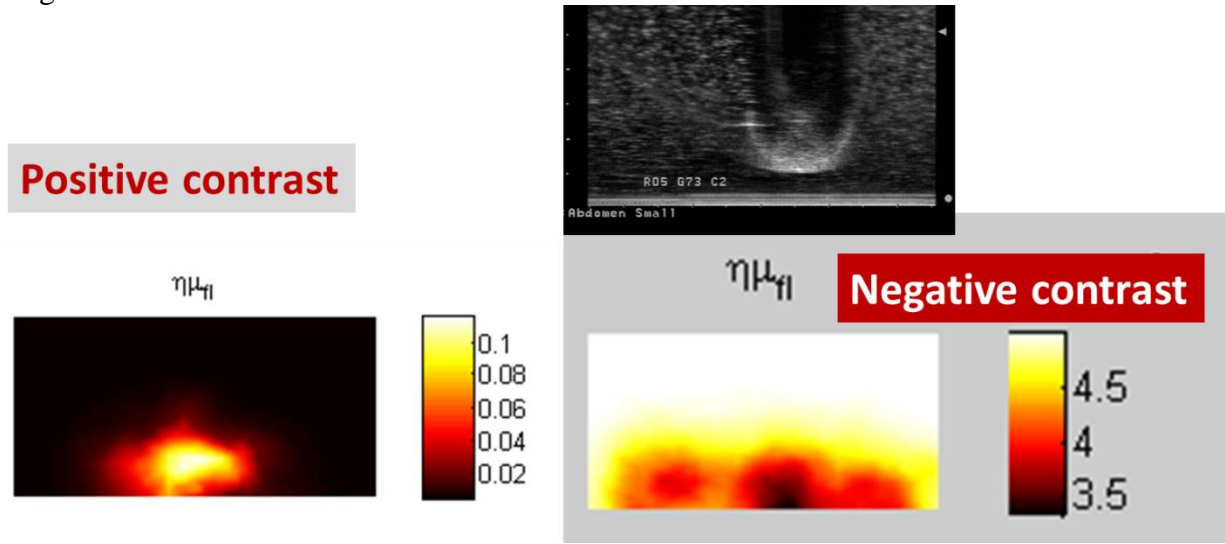


Figure 14. TRUS-coupled FDOT measurement. Top panel: a TRUS image of the negative-contrast tissue phantom. Lower left: the reconstructed image for the target having a positive-contrast of fluorescence over the background. Lower right; the reconstructed image for the target to have a negative-contrast of the fluorescence over the background.

### 3. KEY RESEARCH ACCOMPLISHMENTS DURING YEAR 2

Expanding to the year-2 of this project, we have furthered our understanding of the challenges and feasibilities of trans-rectal FDOT of “negative-contrast” fluorescence. The progresses are made in three aspects: analytical modeling, numerical study, and experimental demonstration.

- A novel analytical approach has been developed to quantify the diffuse photon propagation in an outward-imaging geometry that idealizes transrectal optical imaging. This analytical approach is also the first of its kind that applies to both outward-imaging and in-ward imaging through a cylindrically-shaped medium-applicator interface.
- Numerical studies have demonstrated that DOT/FDOT measurements is less sensitive to a negative-contrast target than to a positive-contrast target, and detecting a target of negative-contrast in the trans-rectal prostate-imaging geometry is especially challenging.

- Experimental works are conducted to test the feasibility of TRUS-coupled FDOT of tissue phantoms containing target of positive or negative fluorescent contrast over the background. "Negative-contrast" target is found very challenging to reconstruct.

#### **4. REPORTABLE OUTCOMES**

The research has lead to the following reportable outcomes.

##### **Journal publications**

- Zhang A, Piao D, Bunting CF, "Photon diffusion in a homogeneous medium bounded externally or internally by an infinitely long circular cylindrical applicator. III. Synthetic-study of continuous-wave photon fluence rate along unique spiral-paths," Journal of the Optical Society of America, A, 29(4): 545-558 (2012).
- Zhang A, Piao D, "Photon diffusion in a homogeneous medium bounded externally or internally by an infinitely long circular cylindrical applicator. IV. Frequency-domain analysis," Journal of the Optical Society of America, A, 29(7): 1445-1458 (2012).
- Piao D, Zhang A, Yao G, Xu G, Daluwatte C, Bunting CF, Jiang Y, Pogue BW, "When is spiral straight?," Optics & Photonics News, 22(12): 24, (2011). "Optics in 2011" special issue (peer-reviewed).

##### **Conference proceeding papers**

- Xu G, Piao D, "A Geometric-differential-sensitivity based reconstruction algorithm improves target-depth localization for trans-luminal outward-imaging diffuse optical tomography," Optical Society of America, Biomedical Optics (BIOMED), Paper BTu2A, Apr. 29-May 02, 2012, Miami, FL.
- Piao D, "Time-domain photon diffusions evaluated on concave and convex cylindrical medium-applicator interfaces show opposite trends of the time to reaching the peak-fluence rate---An analytic model," Optical Society of America, Biomedical Optics (BIOMED), Paper BTu3A.67, Apr. 29-May 02, 2012, Miami, FL.
- Zhang A, Piao D, "Effects of heterogeneity to continuous-wave photon remission along unique straight-line equivalent spiral-paths on a long cylindrical medium-applicator interface," Optical Society of America, Biomedical Optics (BIOMED), Paper BTu3A.69, Apr. 29-May 02, 2012, Miami, FL.

##### **PhD dissertation**

- Xu G, "Enhancement of near-infrared diffuse optical tomography for prostate cancer imaging", Oklahoma State University

##### **Course works and research compliance training**

- The trainee-PI Zhang has completed the on-line training modules of "Working with the IACUC Curriculum" and "Human Research Curriculum" administered by the Collaborative Institutional Training Initiative (CITI) (on-line completion report attached).
- The trainee-PI Zhang has also completed an on-site IACUC training administered by the Animal Care and Use Committee of Oklahoma State University (the completion certificate is attached. The date on the certificate is typed incorrectly)

- The continuing trainee-PI Zhang has enrolled in the course “Pattern Recognition and Machine Learning” offered by School of Electrical and Computer Engineering in Fall 2012 semester, to fulfill the course-training plan.
- Both the original trainee-PI Xu and the continuing trainee-PI Zhang have presented to the PhD Seminar Series of School of Electrical and Computer Engineering, to fulfill the career training plan. Xu presented a topic of “Computational modeling on near-infrared diffuse optical tomography for prostate cancer imaging”. Zhang presented a topic of “Using optics to ‘see’ into the tissue.”

## 5. CONCLUSIONS

In conclusion, analytical, numerical, and experimental progresses in year-2 have substantially advanced our understanding of the challenges pertinent to trans-rectal FDOT of negative-contrast fluorescence probe.

## REFERENCES

1. V. Zaichick, T. Sviridova, and S. Zaichick, "Zinc concentration in human prostatic fluid: Normal, chronic prostatitis, adenoma and cancer," *International Urology and Nephrology* **28**, 687-694 (1996).
2. J.S. Reynolds, T.L. Troy, R.H. Mayer, A.B. Thompson, D.J. Waters, K.K. Cornell, P.W. Snyder, and E.M. Sevick-Muraca, "Imaging of spontaneous canine mammary tumors using fluorescent contrast agents," *Photochem. Photobiol.* **66**, 87-94 (1999).
3. S. Achilefu, R. Dorshow, J. Bugaj, and R. Rajagopalan, "Novel receptor-targeted fluorescent contrast agent for in vivo tumor imaging," *Invest. Radiol.* **35**, 479-485 (2000).
4. E. Kuwana and E.M. Sevick-Muraca, "Fluorescence lifetime spectroscopy for pH sensing in scattering media," *Anal. Chem.* **75**, 4325-4329 (2003).
5. A. Godavarty, M.J. Eppstein, C.Y. Zhang, S. Theru, A.B. Thompson, M. Gurfinkel, and E.M. Sevick-Muraca, "Fluorescence-enhanced optical imaging in large tissue volume using a gain-modulated ICCD camera," *Phys. Med. Biol.* **48**, 1701-1720 (2003).
6. V. Ntziachristos, J. Ripoll, L.V. Wang, and R. Weissleder, "Looking and listening to light: the evolution of whole-body photonic imaging," *Nat. Biotech.* **23**, 13-20 (2005).
7. A. Corlu, R. Choe, T. Durduran, M.A. Rosen, M. Schweiger, M.D. Schnall, and A.G. Yodh, "Three-dimensional in vivo fluorescence diffuse optical tomography of breast cancer in humans," *Opt. Express* **15**, 6696-6716 (2007).
8. J. Tian, J. J. Bai, X.-P. Yan, S.-L. Bao, Y.-H. Li, W. Liang, and X. Yang, "Multimodality molecular imaging," *IEEE Trans. Med. Biol. Mag.* **27**, 48-57 (2008).
9. A. Hagen, D. Grosenick, and R. Macdonald, "Late-fluorescence mammography assesses tumor capillary permeability and differentiates malignant from benign lesions," *Opt. Express* **17**, 17016-17033 (2009).
10. S. van de Ven, A.J. Wiethoff, T. Nielsen, B. Brendel, M. van der Voort, R. Nachabe, M. van de Mark, M. van Beek, L. Nakker, L. Fels, S. Elias, P. Luijten, and W. Mali, "A novel fluorescent imaging agent for diffuse optical tomography of the breast: first clinical experience in patients," *Mol. Imaging Biol.* **12**, 343-348 (2010).
11. F. Gao, J. Li, L.-M. Zhang, P. Poulet, H.-J. Zhao, and Y. Yamada, "Simultaneous fluorescence yield and lifetime tomography from time-resolved transmittances of a small-animal-stimulating phantom," *Appl. Opt.* **49**, 3163-3172 (2010).

12. A. Leproux, M. van der Voort, M.B. van der Mark, R. Harbers, S.M.W.Y. van de Ven, and T.G. Van Leeuwen, "Optical mammography combined with fluorescence imaging: lesion detection using scatterplots," *Biomed. Opt. Express* **2**, 1007-1020 (2011).
13. D. Piao, H. Xie, W. Zhang, J.S. Kransinski, G. Zhang, H. Dehghani, and B.W. Pogue, "Endoscopic, rapid near-infrared optical tomography," *Opt. Lett.*, **31**(19): 2876-2878 (2006).
14. A. Ishimaru, "Diffusion of light in turbid material," *Appl. Opt.*, **28**, 2210-2215 (1989).
15. S. Fantini, M.A. Franceschini, and E. Gratton, "Semi-infinite-geometry boundary problem for light migration in highly scattering media: a frequency-domain study in the diffusion approximation," *J. Opt. Soc. Am. B*, **11**, 2128-2138 (1994).
16. Srinivasan S, Pogue BW, Carpenter C, Jiang S, Wells WA, Poplack SP, Kaufman PA, Paulsen KD., "Developments in quantitative oxygen-saturation imaging of breast tissue in vivo using multispectral near-infrared tomography," *Antioxid Redox Signal.*; **9**(8):1143-56 (2007). Review.
17. A. Sassaroli, F. Martelli, G. Zaccanti, and Y. Yamada, "Performance of fitting procedures in curved geometry for retrieval of the optical properties of tissue from time-resolved measurements," *Appl. Opt.* **40**, 185-197 (2001).
18. A. Zhang, D. Piao, C.F. Bunting, B.W. Pogue, "Photon diffusion in a homogeneous medium bounded externally or internally by an infinitely long circular cylindrical applicator. I. Steady-state theory," *J. Opt. Soc. America, A*, **27**(3): 648-662 (2010).
19. A. Zhang, G. Xu, C. Daluwatte, G. Yao, C.F. Bunting, B.W. Pogue, D. Piao, "Photon diffusion in a homogeneous medium bounded externally or internally by an infinitely long circular cylindrical applicator. II. Quantitative examination of the steady-state theory," *J. Opt. Soc. America, A*, **28**(2): 66-75 (2011).
20. D. Piao, A. Zhang, G. Yao, G. Xu, C. Daluwatte, C.F. Bunting, Y. Jiang, B.W. Pogue, "When is spiral straight?," *Optics & Photonics News*, **22**(12): 24, (2011). "Optics in 2011" special issue (peer-reviewed).
21. Zhang A, D. Piao, C.F. Bunting, "Photon diffusion in a homogeneous medium bounded externally or internally by an infinitely long circular cylindrical applicator. III. Synthetic-study of continuous-wave photon fluence rate along unique spiral-paths," *J. Opt. Soc. America, A*, **29**(4): 545-558 (2012).
22. A. Zhang, D. Piao, "Photon diffusion in a homogeneous medium bounded externally or internally by an infinitely long circular cylindrical applicator. IV. Frequency-domain analysis," *J. Opt. Soc. America, A*, **29**(7): 1445-1458 (2012).
23. H. Dehghani, M. E. Eames, P. K. Yalavarthy, S. C. Davis, S. Srinivasan, C. M. Carpenter, B. W. Pogue, and K. D. Paulsen, "Near infrared optical tomography using NIRFAST: Algorithm for numerical model and image reconstruction," *Communications in Numerical Methods in Engineering* **25**, 711-732 (2009).
24. Jiang, Z., Piao, D., Holyoak, G. R., Ritchey, J. W., Bartels, K. E., Slobodov, G., Bunting, C. F. & Krasinski, J. S. Trans-rectal Ultrasound-coupled Spectral Optical Tomography of Total Hemoglobin Concentration Enhances Assessment of the Laterality and Progression of a Transmissible Venereal Tumor in Canine Prostate. *Urology* **77**, 237-242 (2011).
25. He J, Weersink RA, Veilleux I, Piao D, Trachtenberg J, Wilson BC, "Development of transrectal diffuse optical tomography combined with 3D-transrectal ultrasound Imaging to monitor the photocoagulation front during interstitial photothermal therapy of primary focal prostate," *SPIE International Symposium on Biomedical Optics*, Feb. 02-07, 2013, San Francisco, CA. Paper 8578-56.



# CITI Collaborative Institutional Training Initiative (CITI)

## Working with the IACUC Curriculum Completion Report Printed on 5/18/2012

**Learner:** Anqi Zhang (username: AndrewZhang)

**Institution:** Oklahoma State University

**Contact Information** Department: Electrical and Computer Engineering

Phone: 4057446511

Email: anqi.zhang@okstate.edu

**Working with the IACUC:** The CITI Basic Course in Laboratory Animal Welfare for Investigators, Staff and Students.

### Stage 1. Basic Course Passed on 05/18/12 (Ref # 7951951)

Required Modules	Date Completed	
Introduction to Working with the IACUC	05/18/12	no quiz
Working with the IACUC	05/18/12	3/3 (100%)
The Veterinary Consultation	05/18/12	1/1 (100%)
Getting Started	05/18/12	5/5 (100%)
Alternatives	05/18/12	8/8 (100%)
Avoiding Unnecessary Duplication	05/18/12	1/1 (100%)
USDA Pain/Distress Categories	05/18/12	8/8 (100%)
Personnel Training and Experience	05/18/12	3/3 (100%)
Occupational Health and Safety	05/18/12	1/1 (100%)
Euthanasia	05/18/12	5/5 (100%)
Making Changes after You Receive Approval	05/18/12	1/1 (100%)
Reporting Misuse, Mistreatment, or Non-Compliance	05/18/12	no quiz
Final Comments	05/18/12	no quiz

**For this Completion Report to be valid, the learner listed above must be affiliated with a CITI participating institution. Falsified information and unauthorized use of the CITI course site is unethical, and may be considered scientific misconduct by your institution.**

Paul Braunschweiger Ph.D.  
Professor, University of Miami  
Director Office of Research Education  
CITI Course Coordinator

[Return](#)



# CITI Collaborative Institutional Training Initiative

## Human Research Curriculum Completion Report Printed on 5/18/2012

**Learner:** Anqi Zhang (username: AndrewZhang)

**Institution:** Oklahoma State University

**Contact Information** Department: Electrical and Computer Engineering

Phone: 4057446511

Email: anqi.zhang@okstate.edu

**Biomedical Research Investigator Faculty /Staff/Student:**

**Stage 1. Basic Course Passed on 05/18/12** (Ref # 7951950)

Required Modules	Date Completed	
Introduction	05/18/12	no quiz
History and Ethical Principles	05/18/12	6/6 (100%)
Basic Institutional Review Board (IRB) Regulations and Review Process	05/18/12	5/5 (100%)
Informed Consent	05/18/12	4/4 (100%)
Privacy and Confidentiality - SBR	05/18/12	5/5 (100%)
Social and Behavioral Research for Biomedical Researchers	05/18/12	4/4 (100%)
Records-Based Research	05/18/12	2/2 (100%)
Research With Protected Populations - Vulnerable Subjects: An Overview	05/18/12	4/4 (100%)
Conflicts of Interest in Research Involving Human Subjects	05/18/12	5/5 (100%)
Oklahoma State University module	05/18/12	no quiz

**For this Completion Report to be valid, the learner listed above must be affiliated with a CITI participating institution. Falsified information and unauthorized use of the CITI course site is unethical, and may be considered scientific misconduct by your institution.**

Paul Braunschweiger Ph.D.  
Professor, University of Miami  
Director Office of Research Education  
CITI Course Coordinator

[Return](#)

# *IACUC Training Certificate*

Anqi Zhang

<i>ID</i>	<i>Type of Training</i>	<i>Required Frequency</i>	<i>Date Taken</i>	<i>Renewal Date</i>
1401	OSU IACUC Training	Triennial	9 /17/2912	9 /17/2915